2.3 THE CRYSTAL STRUCTURE, ORIENTATION RELATIONSHIPS AND INTERFACES OF THE NANOSCALE OXIDES IN NANOSTRUCTURED FERRITIC ALLOYS —

Y. Wu , S. Kraemer, G. R. Odette (University of California Santa Barbara), J. Ciston (Lawrence Bekeley National Laboratory), N. Bailey, P. Hosemann (University of California Berkeley)

OBJECTIVES

The objective of this study is to use aberration-corrected high-resolution transmission electron microscopy to characterize the nanoscale oxides in four NFA conditions, including severe deformation and extreme neutron radiation exposure.

SUMMARY

Fast Fourier Transform analysis of focal series images revealed the nano-oxide (NO) crystal structure, including the smallest at < 2 nm in diameter, to be $Y_2Ti_2O_7$ pyrochlore in all cases, consistent with both exit wave analysis and scanning transmission Z-contrast imaging of the atomic columns in larger features. The faceted NOs exhibit a quasi-epitaxial orientation relationship to the ferrite matrix: $[110]_{YTO}||[100]_{Fe}$ and $[001]_{YTO}||[010]_{Fe}$, forming a 5x7 near coincidence site interface, and exhibit size-dependent strains in both the oxide and matrix ferrite phases.

BACKGROUND

Fusion reactors will require advanced materials with tolerance to intense high-energy neutron fluxes that generate helium concentrations reaching thousands of atomic parts per million and hundreds of atomic displacements per atom over the operating lifetime. Neutron damage leads to void swelling, embrittlement and irradiation creep [1-3]. Managing helium is a grand challenge for turning the promise of C-free fusion power into a reality. Nanostructured ferritic alloys (NFAs) are promising candidate materials, which are dispersion strengthened by an ultrahigh density (≈ $5x10^{23}/m^3$) of Y-Ti-O nano-oxides (NOs) averaging ≈ 2.5 nm in diameter, with volume fractions of ≈ 0.75% [1-3]. NOs result in unique irradiation tolerance because they pin dislocations, help to self-heal vacancy and self-interstitial damage; and, most significantly, trap otherwise highly damaging helium in harmless nm-scale interface bubbles [1-3]. Notably, NFAs can manage very high concentrations of transmutation product helium produced in fusion reactors. Thus understanding of NOs is essential to developing, qualifying and optimizing NFAs.

PROGRESS AND STATUS

Experimental Procedure

Alloy information

The TEM studies were carried out on three conditions of NFA MA957 and a 14YWT heat recently developed in the DOE Fuel Cycle Research and Development Program called FCRD NFA-1. The variants of MA957 included as-extruded (AE), friction stirred weld and annealed (FSWA), and irradiated (IR) conditions. The AE MA957 was obtained from Pacific Northwest National Laboratory in the form of extruded 25-mm-diameter rods [4]. The FSW was prepared by Edison Welding Institute in collaboration with UCSB, by joining two MA957 AE coupons, followed by post-weld annealing at 1150°C for 1h [5,6]; annealing was intended to relax residual stresses and to recover any potential damage to the NOs that might be caused by severe plastic deformation. The IR condition is another MA957 heat irradiated to 109 dpa at 412°C in the Fast Flux Test Reactor [7]. FCRD NFA-1 is a best practice heat of 14YWT in the form of an extruded and cross-rolled plate [8]. Various combinations of APT, SANS, TEM and mechanical property measurements have been used to extensively characterize these four NFA conditions; further details can be found in [5-8, 9-11].

TEM characterization

Electron transparent TEM specimens were prepared by either the focused ion beam (FIB) lift-out technique, using FEI Helios and Quanta microscopes, or by wedge polishing, followed by ion-milling, both at successively lower energies down to 2kV to minimize the gallium and argon ion damage. Most of the HRTEM images were recorded using the TEAM 0.5 FEI-Titan-class microscope with aberration correction to third order in both TEM and STEM modes [12]. HRTEM data was collected at 300 kV using monochromation to 0.1 eV with the corrector tuned to optimize bright atom contrast (C3 = -6 um, C5 = 2.5mm) and recorded on a 2048x2048 pixel CCD camera. Focal series were recorded with a defocus step of -1.72 nm ranging from -34.4 nm under focus to 34.4 nm over focus. Exit wave reconstruction was performed using the Gershberg-Saxton algorithm [13] as implemented in the MacTempasX software [14]. Exit wave reconstruction is a holographic technique that can provide both the amplitude and phase of the electron wave after passing through the sample. Once the complex wave is known, all residual aberrations of the microscope can be corrected in software [15], improving the interpretability of the HRTEM data. Furthermore, at the limit of the weak phase object approximation, the exit wave phase is directly related to the projected potential of the object. MacTempasX was also used to perform multi-slice HRTEM simulations using the experimental parameters and a cutoff frequency of 10/nm. Atomic coordinates of the Fe- $Y_2Ti_2O_7$-Fe slab are provided in Supplemental Materials. TEAM 0.5 was also used in STEM mode to record high angle annular dark field (HAADF) images with a 17.1 mrad convergence semi-angle and a collection semi-angle ranging from 75-150 mrad. Finally, electron energy loss spectroscopy (EELS) was used to characterize Ti-profiles for a limited number of NOs. The HRTEM images and exit waves were analyzed by FFT power spectrum lattice indexing. Individual FFT were first calculated and then collectively averaged using MATLAB. The lattice spacing's and inter-planar angles were measured using Image J.

Results

The microstructures of the 4 NFA conditions were characterized by aberration corrected TEM: MA957 in as-extruded (AE), friction stir welded and annealed (FSWA) and irradiated (IR) conditions; and a new developmental heat of 14YWT (NFA-1). Note that the FSWA and IR conditions represent extreme conditions of deformation and neutron irradiation exposure, respectively. Figure 1a is a bright field TEM image of the MA957 FSWA condition, showing the NO features. The NOs have elongated cuboidal shapes with sizes widely ranging from ≈ 1 to 12 nm.

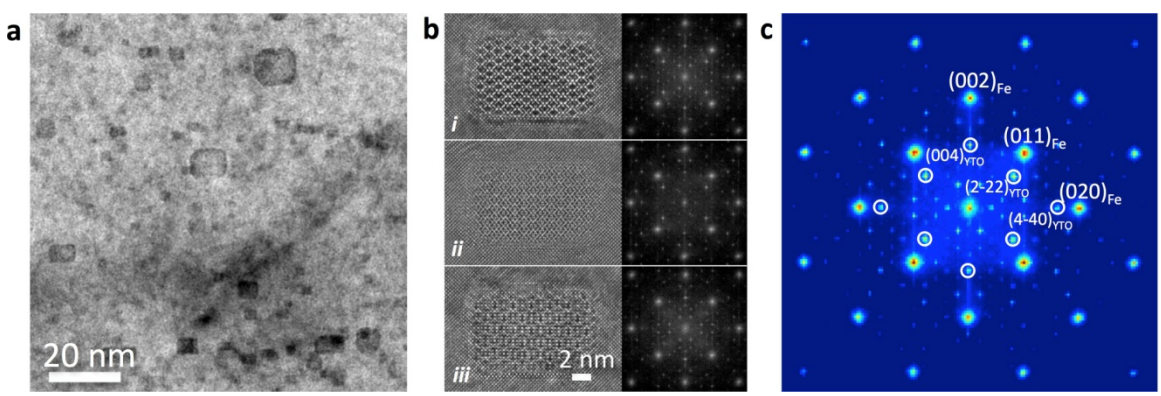

Figure 1. a) A bright field TEM image at low magnification of FSWA MA957 showing faceted, cuboidal oxide particles with a wide size distribution; b), representative HRTEM images from the focal series for a large NO and the corresponding power spectra for: i) under-; ii) near; and, iii) over-focus; and, c), the averaged FFT from all HRTEM images of the NO shown in Figure 1b, where the larger high-intensity reflections and their multiples are from the Fe-Cr ferrite matrix (Fe) while the white circles mark the major reflections of $Y_2Ti_2O_7$ pyrochlore (YTO) with corresponding zone axes of $[100]_{Fe}$ and $[110]_{YTO}$.

The left side of Figure 1b shows three HRTEM images of the same NO, as examples of a larger series representing (i) under-; (ii) close-to-; and, (iii) over-focused conditions. The NO is sharply faceted and the Moiré patterns indicate that it is crystalline. The right side of the Figure 1b shows the associated FFT for each of these focal condition examples. The overlay of stronger and weaker lattice spots represent reflections of the ferrite matrix and the NO, respectively. The weak NO reflections vary in amplitude with the focal condition and, in some cases, even disappear. This is a result of the strong image modulations introduced by the contrast transfer function of the TEM objective lens.

Taking the average over all fast Fourier transforms (FFTs) in a focal series minimizes contrast transfer function effects and provides a higher signal-to-noise ratio. The corresponding averaged FFT is shown in Figure 1c. The strong reflections (with a red spot in the middle) are the <100> zone-axis pattern of the bcc ferrite matrix. The primary reflections from the NOs, marked by white circles, are consistent with $Y_2Ti_2O_7$ pyrochlore with a <110>-zone axis. Detailed analysis shows that all other spots arise from multiple scattering.

The in-focus electron wave phase obtained from exit-wave reconstruction (EWR) in Figure 2 takes into account the transfer function modulations, and provides a more interpretable representation of the projected crystal structure.

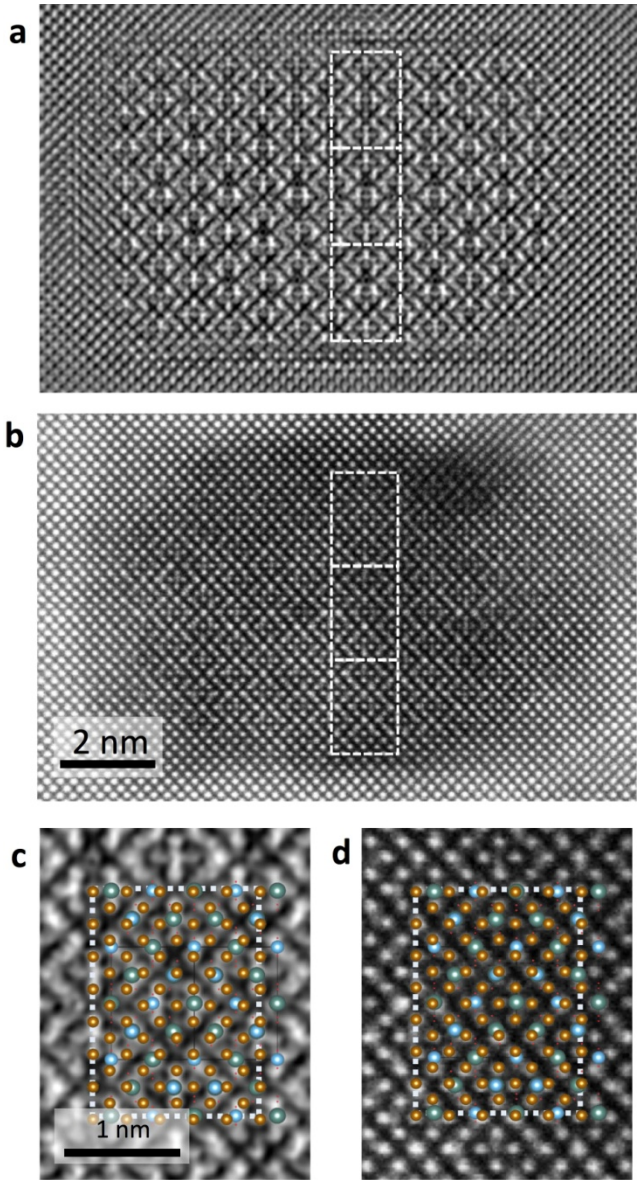

Figure 2. a). The phase of the reconstructed exit wave from of the focal series in Figure 1b. b) the corresponding HAADF STEM image where the dashed lines highlight the periodicity of the Moiré pattern in the overlap region. c) magnified views of the periodic structure in the exit-wave reconstruction image, and d), in the corresponding HAADF STEM image. The dashed lines show the periodic repeated pattern of 5x7 Fe unit cells, while the colored balls represent lateral positions of Y (green) and Ti (blue) columns relative to Fe (yellow) matrix.

Figure 2a displays the phase of the reconstructed HRTEM exit wave, with white atom contrast, while Figure 2b shows the corresponding HAADF STEM image. In both cases a periodic image pattern is observed in the central region of the large NO, reflecting the overlap of the ferrite matrix and the $Y_2Ti_2O_7$ pyrochlore crystal structures. The in-focus phase of the exit wave and HAADF STEM images are both interpreted as projected atomic columns, as supported by corresponding HRTEM simulations (not shown here). Corresponding overlays of an ideal $Y_2Ti_2O_7$ pyrochlore atomic model with the observed OR are shown in Figures 2c and 2d. The dashed lines correspond to a periodic array of 5x7 Fe periodic cells, while the colored balls represent lateral positions of Y (green) and Ti (blue) atoms relative to the Fe matrix

(yellow), based on a visual best fit position adjustment of the image intensities. Note the visible atoms represent columns of pure Y, pure Ti and mixed Y and Ti. The bulk $Y_2Ti_2O_7$ model is very well matched to the EWR and STEM column patterns, when displaced relative to the ferrite matrix, based on simple visual pattern matching. The periodic pattern corresponds to a 5x7 Fe periodic cell near coincident site lattice.

A HAADF STEM image of AE MA957 is shown Figure 3a. The faceted oxides are significantly smaller in this case, many less than 2 nm. Clearly imaging the smallest NOs in HRTEM is very difficult due to reduced atomic mass contrast, the dominance of interfaces, as well as the possibilities of complex chemical oxide terminations, mismatch strains, solute segregation and the presence of both ferrite matrix lattice and oxide defects. The averaged FFT of one somewhat larger NO in the AE condition, shown in Figure 3b, deviates from those in for the FSWA MA957 in Figure 1c, since there are {100} indexed spots lying on a line between the major {110} type Fe reflections, which would be forbidden in an ideal bulk crystal. These extra spots may occur due to a symmetry-breaking sharp truncation of the bcc Fe crystal at the small NOs interface and possible lattice defects. The other reflection spots visible on the line between the Fe reflections are consistent with a $Y_2Ti_2O_7$ pyrochlore crystal orientated along [100] with a $[100]_{YTO}$ || $[010]_{Fe}$ and $[011]_{YTO}$ || $[100]_{Fe}$ OR, which is also found by both Dawson et al.[16] and Ribis et al. [17].

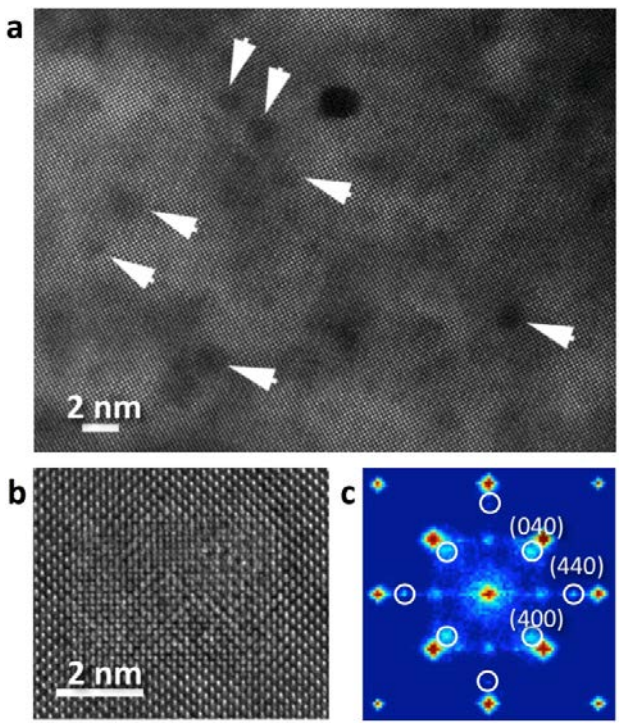

Figure 3. TEM images for AE MA957: a) a HAADF STEM overview image with arrows marking some oxide particles; b) a HRTEM image of a larger particle; and, c) an averaged FFT of all the images in the corresponding focal series. White circles mark the major reflections of $Y_2Ti_2O_7$ pyrochlore (YTO). The corresponding zone axes are $[100]_{Fe}$ and $[001]_{YTO}$.

Structural information was also obtained from the extra spots in the FFT for a larger image area containing a sufficient volume fraction of NOs, even if they could not be individually indexed due to signal to noise limitations for individual embedded NOs. Note that in the MA957 IR condition, the individual NOs were not indexed, but this will be part of future research. The collage in Figure 4 is a summary of corresponding power spectra for all the NFA conditions in this study. Each spectrum is based on the average of all the individual images in the focal series. For comparison purposes, Figure 1c is repeated in 4a. Figures 4b and 4c are power spectra from two other regions in FSWA MA957. Figure 4b is for a NO that is 1.8 nm high and 3.2 nm wide. The large aspect ratio can be seen as an elongation of the corresponding reflections along the vertical axis. Due to the smaller size of these NOs, multiple scattering

is reduced compared to the larger crystal shown in Figure 1a. The Fe region next to the particle contains no discernible features. The corresponding FFT in Figure 4c mainly contains ferrite matrix spots, with only very minimal indications of any other structures in the background.

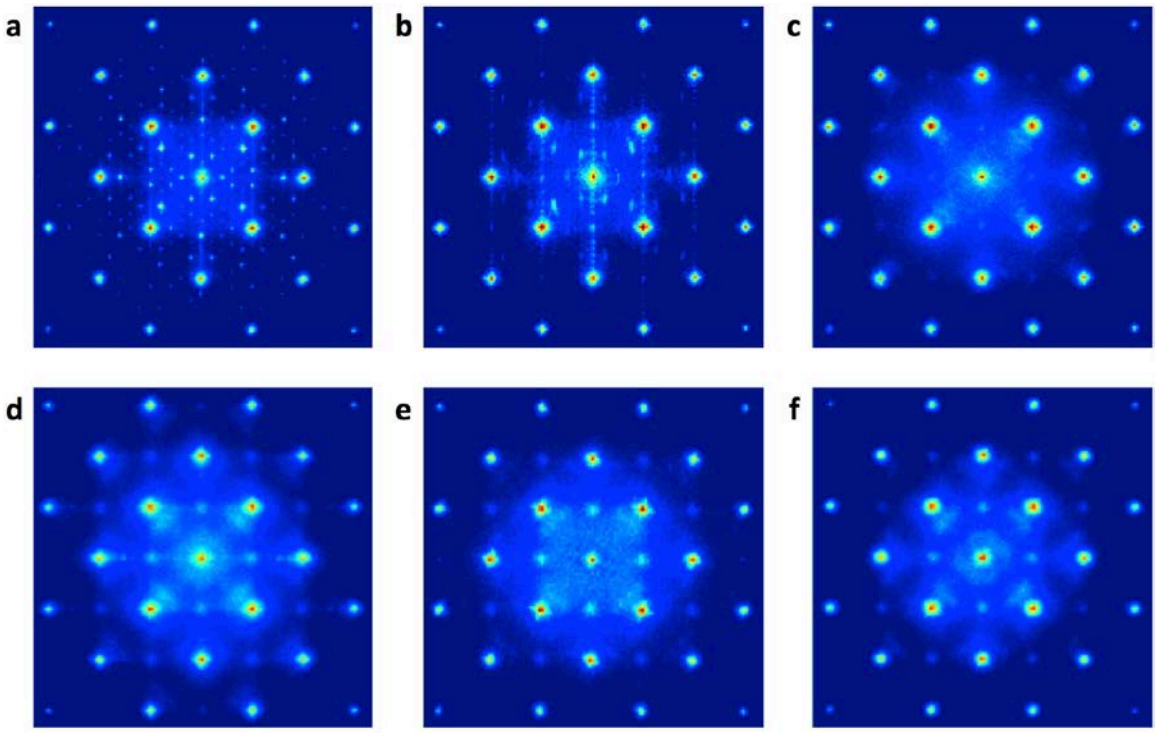

Figure 4. A summary of the averaged FFTs for all the NFA conditions studied. The top row is the FSWA MA957 for: a) the large NO shown in Figure 1c; b) a smaller 3.2x1.8 nm^2 NO; and c) the area next to the small NO in b. The bottom row is for MA957 in the: d) AE MA957; e) IR MA957 conditions; and f) NFA-1.

Figures 4d and 4e are FFT for the AE and IR MA957 conditions, respectively, and Figure 4f is for NFA-1. All the FFT for a larger area of the foil show the same characteristic extra spot features, i.e. weak peaks in between and close to the {200}-type Fe reflections. The spots near the Fe peaks are at the same locations that were previously assigned to $Y_2Ti_2O_7$ pyrochlore in Figure 1. The detailed analysis results of Figure 3 and Figure 4 are summarized in Table 1. Note Ribis et al. also reported pyrochlore structure is stable after irradiation [17]. However, in contrast to the other images, these spots are streak-like broadened, as discussed in the next section.

A careful analysis of NOs in MA957 and 14YWT NFA-1 heat reveals strongly facetted shapes and a well-defined OR to the ferrite matrix. All of the recorded and indexed power spectra are consistent with a *cube-on-edge* OR as illustrated in Figure 5a with $[110]_{YTO}$ || $[100]_{Fe}$ and $[001]_{YTO}$ || $[010]_{Fe}$ for all of the alloy conditions.

Table 1. Summary of d-spacing's and plane angles measured in the indicated figures compared to bulk $Y_2Ti_2O_7$

Figure	d (Å)	d_1(2-22)	d_2(22-2)	α_{12}(°)
Fig. 4d	Measured	2.83±0.09	2.83±0.09	68.7±0.9
Fig. 4e	Measured	2.85±0.07	2.85±0.07	71.9±1.3
Fig. 4f	Measured	2.81±0.07	2.80±0.07	69.4±1.8
	$Y_2Ti_2O_7$	2.90	2.90	70.5
Fig. 3c	d (Å)	d_1(400)	d_2(040)	α_{12}(°)
	Measured	2.60±0.08	2.60±0.08	90.6±1.8
	$Y_2Ti_2O_7$	2.52	2.52	90

Due to the two-fold symmetry of the <110>-zone axis there are three possible variants of overlapping ferrite and $Y_2Ti_2O_7$ pyrochlore diffraction patterns. Figure 5b i) shows possible peak locations in the power spectrum assuming an equal mix of three cube-on-edge rotations. Figures 5b ii) and iii) correspond to <110>-type $Y_2Ti_2O_7$ pyrochlore patterns rotated 90°, while iv) shows a <100>-type pattern that is 45° rotated relative to $[100]_{Fe}$. Notably, Figures 4d, 4e and 4f show streaking of the corresponding $Y_2Ti_2O_7$ reflections that are consistent with a combination of these three rotation variants.

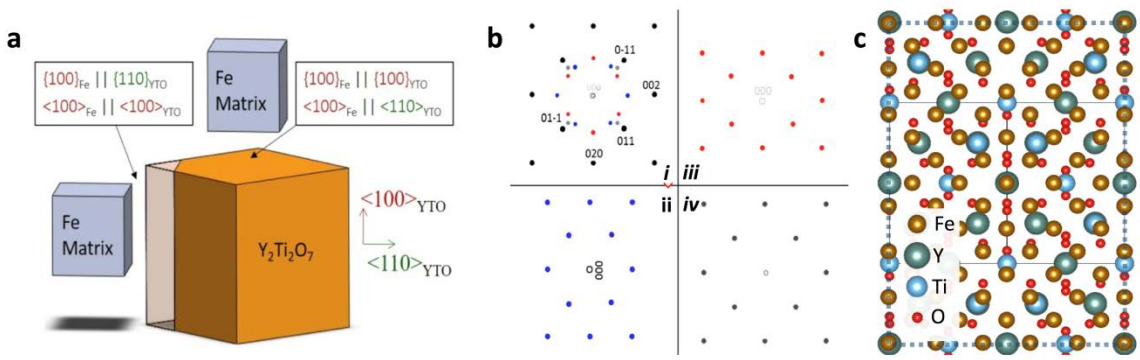

Figure 5. a) A schematic illustration of the cube on edge OR of $Y_2Ti_2O_7$ pyrochlore (small cube) relative to the Fe matrix (large cube); b) i) all possible peak locations in the FFT assuming a cube-on-edge OR where ii) and iii) represent $<110>_{YTO}$ orientations rotated with respect to each other by 90° and, iv) is $<100>_{YTO}$ rotated 45° around the zone axis. c) The 5 x 7 array of Fe matrix unit cells in near-coincidence periodicity with the $Y_2Ti_2O_7$ pyrochlore (cation) lattice.

The strong OR between ferrite matrix and $Y_2Ti_2O_7$ pyrochlore is intriguing given the incommensurate bulk unit cells of the two crystals. Nevertheless, it is noted that the overlapped crystal structures with the specified OR show a near CSL between Fe atoms and Y and Ti cations that spans 5x7 ferrite periodic cells, as illustrated in Figure 5c. Note, Figure 5c represents an yet to be published first principles calculation of an embedded NO, provided by Y. Jiang at the South Central University In China, which was inspired by the TEM results reported here. The atomic positions, including O, in a 525 atom supercell are fully relaxed from a bulk pyrochlore structure with the 5x7 CSL interface with the ferrite matrix. The first principles minimization resulted in only small movements of the atoms, suggesting that this interface represents a highly stable structure. Details of this very recent modeling research will be the subject of a future publication, including corresponding interface energies, as well as a full oxygen potential and temperature dependent interface phase diagram. These repeat units in Figure 5c correspond exactly to the observed periodicity seen in Figure 2b and the coherent structures are consistent with the EWA. The lattice mismatch is remarkably low across these periodic distances, at only +0.45% along the horizontal and -0.57% along the vertical directions. The corresponding strains in the fully relaxed DFT model are

horizontal/vertical: 1/1.05% in Fe and -1.77/-0.7% in $Y_2Ti_2O_7$. Due to the symmetry of the OR, the lattice strains along horizontal and the third, out of plane, direction are equivalent.

The interfaces between the NO and ferrite matrix are also remarkably flat, as is especially seen in the FSWA condition shown in Figure 1; note the other alloy conditions also show faceted NOs. The example of the larger particle in the MA957 AE condition in Figure 3c is most striking. Nevertheless, upon close inspection one can also recognize similar faceting for the smaller particles. Note that the direction of the arrows in Figure 3a correspond to <100> directions of the ferrite lattice. Presumably optimally matched interfaces between low-energy planes on both the oxide and iron matrix sides are self-selected. However, the exact shape of the particles cannot be determined from the projection images we have obtained and need to be further characterized by electron tomography, for example.

We conclude that: a) the NO are predominantly $Y_2Ti_2O_7$ pyrochlore that persist to small sizes even in the face of severe deformation and extreme irradiation exposure and in all four alloy conditions; b) the NOs observed here have a predominantly cube on edge $[110]_{YTO}$ || $[100]_{Fe}$ and $[001]_{YTO}$ || $[010]_{Fe}$ OR relationship in all conditions; c) the atomic scale interface in a larger NO can be described as a 5x7 near CSL.

A pertinent question is how general are these results? Even wide area TEM FFT measurements only sample a small volume of material. Unfortunately, classical techniques for crystal structure analysis in larger volumes, like XRD, have serious limitations when dealing with low volume fractions of nano-scale crystals, with sizes of order of one to several nm. However, new synchrotron based techniques like the partially or not known structures (PONKS) Rietveld Refinement approach to fit the peak broadened background of the XRD spectra [18] has been recently demonstrated for Ni- Mn-Si nano precipitates in reactor pressure vessel steels at the new NSLS II synchrotron light source at Brookhaven National Laboratory [19]. Application of XRD PONKS to NFAs and NOs will lead to further understanding. Indeed, it is notable that the our preliminary XRD results on AE MA957 show weak peaks and enhanced background that are consistent with the presence of $Y_2Ti_2O_7$ and Y_2TiO_5 NOs, along with much larger TiO features. These results are also consistent with several previous XRD studies that characterized greater volume fractions of larger or extracted NOs [20-22]. Furthermore, a very recent glancing angle XRD study found only $Y_2Ti_2O_7$ peaks in a MA957-like 14YWT NFA [23]. Finally, a combination of SAXS and SANS was used to identify the NOs in another 14YWT alloy, showing that they are consistent with $Y_2Ti_2O_7$ or Y_2TiO_5 [24].

We have focused on the $Y_2Ti_2O_7$ and, in the case of the larger pyrochlore oxide, the detailed atomic structure of its ferrite matrix interface. However, we should emphasize that, as noted above, other oxides are often present in NFAs, and different cube-on-cube ORs have also been reported [25]. Further, while we believe that the HRTEM images suggest that they are similar, we have not resolved the detailed interface structures in the smallest NOs. We also note that in the other limit of µm-scale bilayers of Fe grown on (100) $Y_2Ti_2O_7$ pyrochlore, the edge-on-cube OR is accompanied by interface dislocations with a spacing of 1.4 nm, which are not observed in small embedded NOs that do not experience a semi-infinite in-plane strain condition.

It is useful to emphasize the critical importance of the detailed observations reported here. For example, the presence of interface strains has important implications to the NO interactions with helium. This is especially the case to support modeling efforts to better understand the nature of NOs, their functionality and the corresponding overall performance of NFAs. The first principles result in Figure 5c is an example of the opportunity for close coupling of modeling and experiment. This work also provides “ground truth” to a series of first principles and atomistic studies that have explored: a) initial clustering energetics of Y-Ti-O solutes [26-28]; b) the structure and physical properties of $Y_2Ti_2O_7$ and Y_2TiO_5 [29]; c) the corresponding remarkable ability of NO to sequester helium, in internal interstitial sites and subsequently in associated interface bubbles [30,31]; d) the free surface and embedded interface energies of $Y_2Ti_2O_7$ [32]; and, e) the solubility of Y both in the matrix and at dislocations [33], that mediates the truly

remarkable long-term, high-temperature thermal stability of NOs, as modeled by cluster dynamics methods [4].

A detailed high resolution TEM study was conducted to answer unresolved questions about the nature of the NOs present in NFAs. The results suggest that even the smallest cubic and cuboidal NOs are predominately $Y_2Ti_2O_7$ pyrochlore in all the 14YWT alloy conditions we studied. The NOs have a cube on edge, apparently coherent, interface that manifests a well-ordered 5x7 near CSL oxide-bcc ferrite-matrix boundary structure in a larger oxide. The NOs are under compressive stress while the Fe-matrix is under tension. With the exception of APT measurements, the more detailed results reported here are generally in good agreement with the preponderance of corresponding evidence in the literature although other phases and ORs also occur. The results of this study represent an important step in supporting detailed modeling efforts, such as the first principles simulation of the 5x7 near CSL example in Figure 5c, that will help to develop, optimize and qualify NFA for fusion and advanced fission energy service.

Acknowledgements

Research at UCSB was supported by the Department of Energy Office of Fusion Energy Sciences (Grant No. DE-FG03-94ER54275) and the Office of Nuclear Energy (Grant No. DE-FC07-07ID14825). Most of the specimen preparation and some of the TEM measurements were carried out in the UCSB Materials Research Laboratory Microstructure and Microanalysis Facility, supported by the Materials Research Science and Engineering Center Program of the National Science Foundation under Award No. DMR05-20415. The authors thank our UCSB colleagues P. Wells for insight on APT issues, Dr. T. Yamamoto for his many general contributions to our research program, T. Stan for helpful discussions of the interfaces and many others in the Odette Group for their assistance in various parts of this research. We also acknowledge helpful discussions regarding XRD with D. Sprouster and L. Ecker at BNL, and D. Morgan L. Barnard at the University of Wisconsin for their outstanding modeling insight and Y. Jiang at the Central South University in China sharing the DFT results shown in Figure 5. Electron microscopy experiments were performed at the NCEM facility of the Molecular Foundry, which is supported by the Office of Science, Basic Energy Sciences of the U.S. Department of Energy under Contract DE-AC02-05CH11231. The authors would like to thank M. Libbee and C. Song for their support on TEM sample preparation and training at the Molecular Foundry. Finally, we acknowledge the assistance of M. Toloczko at PNNL in providing the irradiated MA957 characterized in this study and S. Maloy at LANL and D. Hoelzer at ORNL for their role as UCSB collaborators in developing FCRD NFA-1.

References

[1] G. R. Odette, M. J. Alinger, B. D. Wirth, “Recent development in irradiation-resistant steels “, *Annu. Rev. Mater. Res*. 38 (2008) 471-503.
[2] G. R. Odette, “Recent progress in developing and qualifying nanostructured ferritic alloys for advanced fission and fusion applications”, *JOM.* **66** (2014) 24272441.
[3] Y. Dai, G. R. Odette, T. Yamamoto, “Basic aspects of radiation effects in solids/basic aspects of multi-scale modeling”, *Comprehensive Nuclear Material.* 1 - Chap 6, Elsevier 141 (2012).
[4] N. J. Cunningham, Y. Wu, D. Klingensmith, G. R. Odette, “On the remarkable thermal stability of nanostructured ferritic alloys”, *Mater. Sci. & Eng. A.* 613 (2014) 296-305.
[5] P. Miao et al., “The microstructure and strength properties of MA957 nanostructured ferritic alloy joints produced by friction stir and electro-spark deposition welding”, *J. Nuc. Mater.* 367 (2007) 1197-1202.
[6] A. Etienne, N. J. Cunningham, Y. Wu, G. R. Odette, “Effect of friction stir welding and post-weld annealing on nanostructured ferritic alloys”, *Mater. Sci. Technol*. 27 (2011) 724-728.
[7] N. A. Bailey, E. Stergar, M. Toloczko, P. Hosemann, “Atom probe tomography analysis of high dose MA957 at selected irradiation temperatures”, *J. Nuc. Mater.* 459 (2015) 225-234.
[8] N. J. Cunningham, Y. Wu, G. R. Odette, D. T. Hoelzer, S. A. Maloy, “Characterization of a larger best practice heat of 14YWT in annealed powder, HIP consolidated and extruded forms”, *Fusion Reactor Materials Semiannual Progress Report.* DOE/ER-0313/54 (2013) 15-26.

[9] Y. Wu, E. Haney, N. Cunningham, G. R. Odette, "Transmission electron microscopy characterization of the nanofeatures in nanostructured ferritic alloy MA957", *Acta Mater*. 60 (2012) 3456-3468.
[10] D. Bhattacharyya et al., "On the structure and chemistry of complex oxide nanofeatures in nanostructured ferritic alloy U14YWT", *Philos. Mag.* 92 (2012) 2089-2107.
[11] M. J. Alinger, G. R. Odette, D. T. Hoelzer, "On the role of alloy composition and processing parameters in nanocluster formation and dispersion strengthening in nanostructured ferritic alloys", *Acta Mater.* 57 (2009) 392-406.
[12] U. Dahmen et al., "Background, status and future of the transmission electron aberration-corrected microscope project", *Philos. Trans. Royal Soc. A.* 367 (2009) 3795-3808.
[13] R. W. Gerchberg, W. O. Saxton, "Practical algorithm for determination of phase from image and diffraction plane pictures", *Opt*. 35 (1972) 237-246.
[14] R. Kilaas, MacTempasX. http://www.totalresolution.com (2014).
[15] A. Thust, M. Overwijk, W. Coene, M. Lentzen, "Numerical correction of lens aberrations in phase-retrieval HRTEM", *Ultramicroscopy* 64 (1996) 249-264.
[16] K. Dawson, G. J. Tatlock, "Characterization of nanosized oxides in ODM 401 oxide dispersion strengthened steel", *J. Nucl. Mater.* 444 (2014) 252-260.
[17] J. Ribis et al., "Comparison of the neutron and ion irradiation response of nano-oxides in oxide dispersion strengthened materials", J. Mater. Res. 30 (2015) 2210-2221.
[18] N. V. Y. Scarlett, I. C. Madsen, "Quantification of phases with partial or no known crystal structures", *Powder Diffr.* 21 (2006) 278-284.
[19] D. J. Sprouster, J. Sinsheimer, E. Dooryhee et al., "Structural characterization of highly irradiated reactor pressure vessel steels", Accepted in *Scr. Mater.* (2015).
[20] T. Okuda, M. Fujiwara, "Dispersion behavior of oxide particles in mechanically alloyed ODS steel", *Mater. Sci. Lett.* 14 (1995) 1600-1603.
[21] H. Sakasegawa et al., "Precipitation behavior of oxide particles in mechanically alloyed powder of oxide-dispersion-strengthened steels", *J. Alloys and Compd.* 452 (2008) 2-6.
[22] J. R. Rieken et al., "Reactive gas atomization processing for Fe-based ODS alloys", *J. Nuc. Mater*. 428 (2012) 65-75.
[23] A. J. London, B. K. Panigrahi, C. C. Tang, C. Murray, C. R. M. Grovenor, "Glancing angle XRD analysis of particle stability under self-ion irradiation in oxide dispersion strengthened alloys", *Scr. Mater.* 110 (2016) 24-27.
[24] M. Ohnuma et al., "A new method for the quantitative analysis of the scale and composition of nanosized oxide in 9Cr-ODS steel", *Acta Mater.* 57 (2009) 5571-5581.
[25] J. Ribis, Y. de Carlan, "Interfacial strained structure and orientation relationships of the nanosized oxide particles deduced from elasticity-driven morphology in oxide dispersion strengthened materials", Acta Mater. 60 (2012) 238-252.
[26] L. Barnard, G. R. Odette, I. Szlufarska, D. Morgan, "An ab initio study of Ti-Y-O nanocluster energetic in nanostructured ferritic alloys", *Acta Mater.* 60 (2012) 935-947.
[27] Y. Jiang, J. R. Smith, G. R. Odette, "Formation of Y-Ti-O nanocluster in nanostructured ferritic alloys: A first-principles study", *Phys. Rev. B* 79 (2009) 064103.
[28] M. J. Alinger, B. D. Wirth, H. J. Lee, G. R. Odette, "Lattice Monte Carlo simulation of nanocluster formation in nanostructured ferritic alloys", *J. Nuc. Mater.* 367 (2007) 153-159.
[29] Y. Jiang, J. R. Smith, G. R. Odette, "Prediction of structure, electronic and elastic properties of $Y_2Ti_2O_7$ and Y_2TiO_5", *Acta Mater.* 58 (2010) 1536-43.
[30] L. Yang et al., "Trapping Helium in $Y_2Ti_2O_7$ compared to matrix iron: A first principles study." *J. Appl. Phys.* 115 (2014) 143508.
[31] Y. Jin et al., "First principles assessment of helium trapping in Y_2TiO_5 in nano-featured ferritic alloys", *J. Appl. Phys.* 116 (2014) 143501.
[32] L. Yang, Y. Jiang, G. R. Odette, "Nonstoichiometry and relative stabilities of Y_2TiO_7 polar surfaces: A density functional theory prediction" *Acta Mater.* 61 (2013) 7260-7270.
[33] L. Barnard, N. J. Cunningham, G. R. Odette, I. Szlufarska, D. Morgan, "Thermodynamic and kinetic modeling of oxide precipitation in nanostructured ferritic alloys", *Acta Mater.* 91 (2015) 340-354.